PAPER

Check for updates

Exploring the significance of palmitoylation using an artificial protein lipidation system

Kazuki Uchida, [ID] [a] Naofumi Shimokawa, [ID] [b] Rie Wakabayashi, [ID] [a]
Shohei Shiomoto, [ID] [c] Kiyohiro Toyofuku,[a] Nozomu Ogushi,[a] Masahiro Goto, [ID] [ad]
Masaru Tanaka, [ID] [c] Masahiro Takagi [ID] [b] and Noriho Kamiya [ID] *[ad]

Protein lipidation, particularly palmitoylation (attachment of a 16-carbon fatty acid), regulates cellular behaviors by controlling protein function at lipid membranes. In this study, we prepared a series of lipidated green fluorescent proteins ("EGFP–lipids") with various alkyl chain lengths (C8 to C22). Using model lipid membranes and Jurkat (human T lymphocyte) cells, we evaluated how lipidation affects the membrane interactions and vesicular transport from the membrane of these protein–lipid constructs. Our findings demonstrate that elongation of the alkyl chain profoundly affects both lateral membrane diffusion and vesicular transport of the EGFP–lipids. Only artificially lipidated proteins that mimic *in vivo* lipidation exhibited cellular dynamics in response to external signals, which highlights the significance of the natural selection of palmitic acid to maximize the function of proteins on lipid membranes. This insight can also be useful in membrane engineering using artificial protein lipidation techniques, potentially accelerating medical and industrial developments.

Introduction

Protein lipidation, the covalent attachment of lipid molecules to proteins, is a post-translational modification responsible for regulating protein function through membrane association and structural stabilization.[1] There are various types of lipidation, such as acylation, farnesylation, and glycosylphosphatidylinositol modification.[2] *S*-Palmitoylation, a type of *S*-acylation, is a common lipidation, in which palmitic acid (PA) is attached reversibly to specific cysteine residues of proteins by the DHHC (aspartate–histidine–histidine–cysteine) family of palmitoyltransferases (PATs).[3,4] Palmitoylated proteins localize to rafts and caveolae on the plasma membrane, and play an important role in the regulation of signal transduction.[5–7] Rafts are dynamic nanodomains enriched in sphingomyelin and cholesterol, which can include or exclude proteins to varying degrees.[8] Caveolae, a subcategory of rafts, are formed from rafts through the polymerization of caveolin.[9] For example, large-conductance calcium-activated potassium channels, which modulate neuronal excitability and membrane potential in response to both plasma membrane depolarization and intracellular calcium concentration, undergo palmitoylation of the S0–S1 linker, which significantly affects the lateral diffusion of the channels.[10,11] Ras is a monomeric GTPase that acts as a binary molecular switch and regulates cell proliferation and differentiation; its signaling is regulated by palmitoylation and depalmitoylation cycles, which modulate the vesicular transport of Ras between the plasma membrane and cytoplasm.[12,13] Tyrosine kinases of the Src family, which phosphorylate tyrosine residues of other proteins on the cytoplasmic side of the plasma membrane, are unable to localize to rafts or caveolae and mediate signal transduction in the nonpalmitoylated state.[14–16] Thus, accurate, dynamic control of two-dimensional raft/caveolae localization and lateral diffusion of proteins, as well as three-dimensional vesicular transport through palmitoylation, are extremely important in the regulation of protein functions and associated cellular events.

In general, the effect of palmitoylation on the dynamic behavior of proteins has been evaluated by comparing it with that of palmitoylation-deficient mutants introduced by transfection of genetically mutated proteins or by knockdown of PATs using small interfering RNA transfection.[17–19] However, these genetic approaches are unable to control the degree of protein lipidation precisely, which limits them to use in the evaluation of protein behavior in the presence or absence of palmitoylation. Furthermore, it is difficult to track only desired phenomena in complex biological processes in which various molecules are involved because the suppression of

a Department of Applied Chemistry, Graduate School of Engineering, Kyushu University, 744 Motooka, Nishi-ku, Fukuoka 819-0395, Japan. E-mail: kamiya.noriho.367@m.kyushu-u.ac.jp

b School of Materials Science, Japan Advanced Institute of Science and Technology, 1-1 Asahidai, Nomi, Ishikawa 923-1211, Japan

c Institute for Materials Chemistry and Engineering, Kyushu University, 744 Motooka, Nishi-ku, Fukuoka 819-0395, Japan

d Division of Biotechnology, Center for Future Chemistry, Kyushu University, 744 Motooka, Nishi-ku, Fukuoka 819-0395, Japan

© 2025 The Author(s). Published by the Royal Society of Chemistry

RSC Chem. Biol., 2025, **6**, 1483–1496 | 1483

Paper

palmitoylation can affect multiple cellular functions and signaling pathways. Meanwhile, it is worth exploring why nature selects PA as the main lipid for *S*-acylation of proteins to realize varying biological functions through the interaction with lipid membranes.[20]

In our previous report, we established a model system that allows precise control of protein lipidation and multifaceted evaluation of the dynamic behavior of artificially lipidated proteins on rafts and caveolae.[21] Specifically, artificial lipid modification of proteins by ε-(γ-glutamyl)lysine isopeptide bond formation using microbial transglutaminase (MTG)[22–26] enables the stable tethering of genetically-modified proteins of interest with various lipid–peptide substrates. Using this approach, it was shown that artificially palmitoylated enhanced green fluorescent protein (EGFP) was selectively localized to liquid-ordered (L_o) phases, enriched with saturated lipids and cholesterol, formed on giant unilamellar vesicles (GUVs). The palmitoylated EGFP was trafficked into Jurkat cells *via* raft/caveolae-dependent endocytosis in response to immunostimulation with concanavalin A (ConA).

Here, we focused on the effects of the alkyl chain length of lipidated proteins on lipid–lipid interactions and vesicular transport on lipid membranes. In addition to saturated fatty acids from C8 (octanoylation) to C18 (stearoylation), which are the main types observed *in vivo*, long-chain saturated fatty acids (C20 and C22) were enzymatically attached to EGFP *via* a *C*-terminal LQ-tag (amino acid sequence LLQG). These extended acyl chain modifications were introduced to take advantage of our system's capacity to precisely control chain length, thereby allowing us to investigate chain length-dependent thresholds that are difficult to probe using conventional biological approaches. Thus, we generated a series of EGFP–lipid fusions, EGFP–C*n*, where *n* = 8, 10, 12, 14, 16, 18, 20, and 22. By using a hybrid model system consisting of artificial and natural membranes, two-dimensional localization and lateral diffusion of EGFP–lipid fusions on artificial lipid bilayers were evaluated. We also assessed three-dimensional vesicular transport using live cells. Our experiments explore the significance of protein lipidation, in particular palmitoylation.

Results

Interaction of EGFP–lipids with artificial lipid bilayers

First, we investigated the effect of the alkyl chain length of EGFP–lipids on the localization to lipid domains on GUVs [1,2-dioleoyl-*sn*-glycero-3-phosphocholine (DOPC)/1,2-dipalmitoyl-*sn*-glycero-3-phosphocholine (DPPC)/cholesterol = 40:40:20]. GUVs phase separate. Saturated lipids and cholesterol form an L_o phase, and unsaturated lipids form a liquid-disordered (L_d) phase.[27–30] The L_o phase is used as a raft model phase for microscopic observation because of its similarity to the lipid composition of rafts and caveolae. Because rhodamine B 1,2-dihexadecanoyl-*sn*-glycero-3-phosphoethanolamine triethylammonium salt (rhodamine–DHPE) localizes to the L_d phase, the red fluorescent regions in analysis by confocal laser scanning microscopy (CLSM) indicate the DOPC-rich L_d phase,
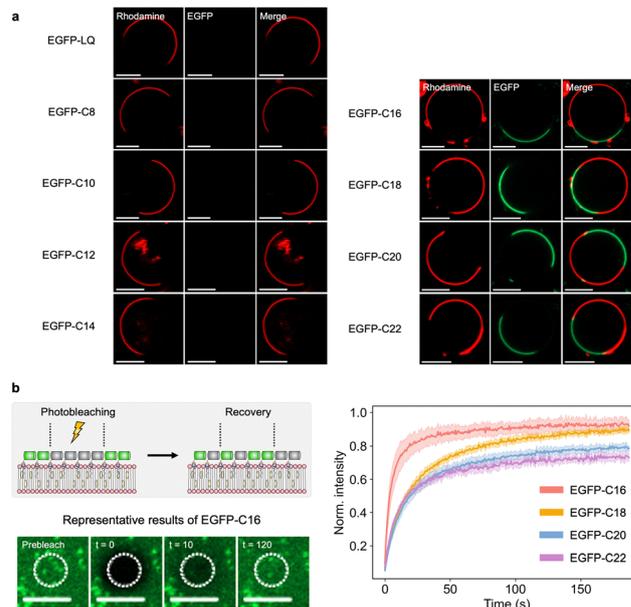
Fig. 1 Association of enhanced green fluorescent protein (EGFP)–lipids with artificial lipid bilayers. (a) Association of EGFP–lipids with phase-separated giant unilamellar vesicles (GUVs). Representative fluorescence images obtained by confocal laser scanning microscopy (CLSM). The liquid-disordered (L_d) phase consists mainly of 1,2-dioleoyl-*sn*-glycero-3-phosphocholine (DOPC), and the liquid-ordered (L_o) phase consists mainly of 1,2-dipalmitoyl-*sn*-glycero-3-phosphocholine (DPPC) and cholesterol. Phase-separated GUVs were formed with a lipid composition of DOPC/DPPC/cholesterol = 40:40:20. Rhodamine–DHPE was used as a fluorescent probe; the bright and dark regions represent DOPC-rich and DPPC-rich phases, respectively. EGFP–lipids appear in green. (b) Fluorescence recovery after photobleaching experiments on EGFP–lipids on a supported lipid bilayer (DPPC/cholesterol = 60:40). Representative snapshots of EGFP–C16 before and after bleaching. Fluorescence recovery as a function of time for EGFP–C16, −C18, −C20, and −C22 (N = 7). Error bars indicate SD. Scale bars: 5 μm.

while the black regions indicate the DPPC/cholesterol-rich L_o phase.[31] Membrane association of EGFP–LQ and EGFP–lipids modified with saturated fatty acids shorter than PA (*i.e.*, EGFP–C8, −C10, −C12, −C14) was not clearly observed in the conditions of this experiment (Fig. 1a). EGFP–lipids modified with PA and longer saturated fatty acids (*i.e.*, EGFP–C16, −C18, −C20, −C22) were localized to the L_o phase after coincubation with GUVs (Fig. 1a).

Next, the two-dimensional diffusion of EGFP–lipids (EGFP–C16, −C18, −C20, −C22) on a lipid membrane was evaluated by fluorescence recovery after photobleaching (FRAP) experiments on a supported lipid bilayer (SLB). SLBs are conformally coated phospholipid bilayers on solid surfaces and are widely used to study molecular properties on lipid membranes. Lateral diffusion of proteins on lipid membranes is an important factor in regulating plasma membrane dynamics and function.[32] The diffusion of palmitoylated proteins on lipid membranes has been quantitatively evaluated using genetic engineering approaches.[33,34] Here, EGFP–lipids were localized on SLBs consisting of DPPC/cholesterol = 60:40, a composition that forms the L_o phase.[35,36] Fluorescence recovery was monitored

Table 1 Estimated diffusion coefficients (D) and the immobile fraction of EGFP–lipids on a supported lipid bilayer (DPPC/cholesterol = 60 : 40). Data are the mean ± SD

Sample	D ($\mu m^2\ s^{-1}$)	Immobile fraction
EGFP–C16	0.21 ± 0.03	0.08 ± 0.02
EGFP–C18	0.04 ± 0.00	0.02 ± 0.00
EGFP–C20	0.04 ± 0.00	0.15 ± 0.00
EGFP–C22	0.06 ± 0.00	0.25 ± 0.01

after quenching EGFP, in a region where the laser was applied. The fluorescence in the bleached region recovers when EGFP–lipids that were outside the bleached area move into the bleached area (Fig. 1b); thus, the experiments directly measure the dynamics of the EGFP–lipid construct. The results showed a slower fluorescence recovery of EGFP–C18, –C20, and –C22 than of EGFP–C16 (Fig. 1b), and the immobile fraction in the bleached region was found to be increased for EGFP–C20 and –C22 compared with EGFP–C16 and –C18 (Table 1). Elongation of the alkyl chain increased the hydrophobic interaction between the EGFP–lipid and the lipids comprising the SLB, resulting in a decrease in the diffusion coefficient. Furthermore, while the alkyl chain length of the DPPC comprising the SLB matched that of EGFP–C16, longer-chain variants such as EGFP–C18, –C20, and –C22 potentially interacted with the lipid molecules on the substrate-facing leaflet of the SLB (*i.e.*, the monolayer in contact with the solid support), resulting in a large decrease in the diffusion coefficient between EGFP–C16 and –C18.

Interaction of EGFP–lipids with natural lipid bilayers

The effect of the alkyl chain length of EGFP–lipids on three-dimensional movement, including vesicular transport from plasma membranes into the cytoplasm, was investigated. It has been demonstrated that exposure of Jurkat cells, a human acute T-cell leukemia cell line, to the lectin ConA from *Canavalia ensiformis* (jack bean) induces raft-dependent vesicle transport.[37,38] We previously showed that EGFP–C16 is transported into the cell *via* raft/caveolae-dependent endocytosis in response to immunostimulation of Jurkat cells by the addition of ConA.[21] We tracked the endocytic movement of EGFP–lipids by using fluorescently labeled cholera toxin subunit B (CT-B), a pentameric subunit of cholera toxin that binds specifically to ganglioside GM1 localized in rafts and caveolae.

Here, EGFP–lipids at various concentrations were incubated with Jurkat cells, and raft-dependent vesicular transport was induced by the subsequent addition of ConA. EGFP–LQ and EGFP–lipids modified with saturated fatty acids shorter than PA (*i.e.*, EGFP–C8, –C10, –C12, –C14) did not show clear distribution to Jurkat cells in the experimental conditions (Fig. S1). However, EGFP–lipids modified with longer saturated fatty acids (EGFP–C16, –C18, –C20, –C22) exhibited clear distribution to Jurkat cells, and the total fluorescence intensity of EGFP–lipids on plasma membranes and transported into cells was calculated. The fluorescence intensity of EGFP–lipids in and on Jurkat cells was found to increase in an EGFP–lipid
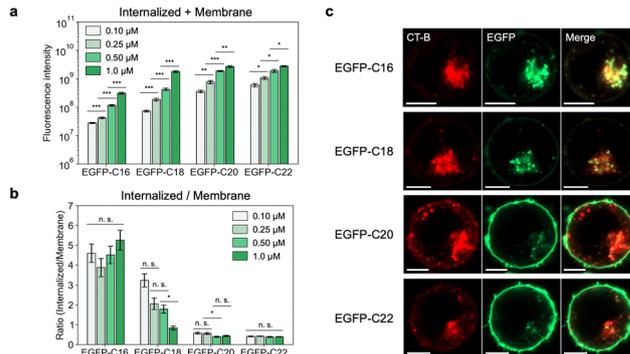
Fig. 2 Association of EGFP–lipids at various concentrations with Jurkat cells, followed by addition of concanavalin A (ConA). (a) Distribution of EGFP–lipids to Jurkat cells (internalized + membrane). (b) Intracellular uptake in response to ConA addition (internalized/membrane) quantified by analyzing fluorescence images obtained by CLSM. $N = 15$; mean ± SE; *$p < 0.05$, **$p < 0.01$, ***$p < 0.001$; ''n.s.'' indicates not significant [Mann–Whitney U-test followed by Bonferroni correction for (a), Kruskal–Wallis test followed by Dunn–Bonferroni *post-hoc* test for (b)]. (c) Representative fluorescence images obtained by CLSM in conditions of comparable total fluorescence intensity from EGFP–lipids with Jurkat cells (internalized + membrane in (a); EGFP–C16, 1.0 μM; EGFP–C18, 0.25 μM; EGFP–C20, 0.1 μM; EGFP–C22, 0.1 μM). Raft and caveolae domains were stained with Alexa Fluor 594-conjugated cholera toxin subunit B (red). EGFP–lipids appear in green. Scale bars: 5 μm.

concentration-dependent manner (Fig. 2a). Elongation of the alkyl chain greatly enhanced the distribution of the lipid to Jurkat cells. Using fluorescence after anchoring of EGFP–lipids at various concentrations to Jurkat cells (Fig. S2a), the ratio of EGFP–lipid internalized into the cell to that on the plasma membrane was calculated. The results indicated that the tendency toward cellular internalization was significantly different depending on the alkyl chain length (Fig. 2b). Interestingly, EGFP–C16 and –C18 colocalized with CT-B inside cells after immune activation by ConA, while EGFP–C20 and –C22 were mostly localized on the plasma membrane. EGFP–C16 was internalized at all the tested concentrations, whereas the internalization of EGFP–C18 was concentration-dependent, showing marked internalization at low concentrations but suppression at higher concentrations. The internalization behavior of EGFP–C20 and –C22 was concentration-independent (Fig. 2b and Fig. S2). Fluorescence images of Jurkat cells with comparable total fluorescence intensities after the coincubation with EGFP–lipids (1.0 μM EGFP–C16, 0.25 μM EGFP–C18, and 0.1 μM EGFP–C20 and –C22) are shown in Fig. 2c. The internalization of EGFP–C16 is evident, whereas the major fractions of EGFP–C20 and –C22 are observed on the plasma membrane. Although EGFP–C18 showed similar behavior to EGFP–C16, the ratio of EGFP–lipid internalized into the cell to that on the plasma membrane was decreased, showing the intermediate behavior of EGFP–C18 between that of EGFP–C16 and EGFP–C20/C22. To rule out the influence of membrane damage by EGFP–lipids on the internalization, the cytotoxicity of EGFP–lipids was assessed. At a concentration of 1 μM, EGFP–lipids bearing alkyl chains from C16 to C22 exhibited a tendency toward increased cytotoxicity with increasing the chain length,

© 2025 The Author(s). Published by the Royal Society of Chemistry

*RSC Chem. Biol.*, 2025, **6**, 1483–1496 | **1485**

although this increase was not statistically significant under the experimental conditions (Fig. S3). These results suggest that the alkyl chain length is a critical factor that determines the behavior of lipid-modified proteins on plasma membranes.

Further biological investigation of the vesicular transport pathway of EGFP–lipids into Jurkat cells was conducted. In a previous study, we demonstrated that depletion of cholesterol in the plasma membrane by preculturing cells with methyl-β-cyclodextrin (MβCD) inhibited internalization of EGFP–C16 *via* a raft/caveolae-dependent endocytosis pathway.[21] However, because MβCD disrupts both raft- and caveolae-dependent pathways, here, we aimed to evaluate the contribution of caveolae-mediated endocytosis more specifically. Caveolae, a subdomain of lipid rafts, are 50–80-nm-sized flask-shaped domains on the plasma membrane, and caveolin-1 (CAV1), which contributes to caveolae formation, is also palmitoylated.[39] Here, knockdown of CAV1 expression by transfection of CAV1 small interfering RNA (siRNA) resulted in a significant decrease in the amount of CAV1 mRNA in Jurkat cells compared with transfection of control siRNA (Fig. S4a). The internalization of EGFP–lipids was evaluated in the same conditions as applied in Fig. 2c (Fig. S4b–e). Knockdown of CAV1 decreased the internalized/membrane-distributed ratio of EGFP–C16 and –C18, indicating a contribution by caveolae-dependent endocytosis to the internalization process (Fig. S4e). However, a substantial amount of EGFP–lipids was still internalized under CAV1 knockdown conditions, suggesting that both raft- and caveolae-dependent endocytosis contribute. No effect of CAV1 knockdown was observed on EGFP–lipid internalization of EGFP–C20 or –C22.

Effect of EGFP–lipid localization on membrane rigidity of Jurkat cells

We aimed to elucidate the underlying mechanism of the inhibition of internalization of proteins with long lipid chains (*e.g.*, C20 and C22 compared with C16; Fig. 2c) by cells. It has been reported that, upon replacement of DPPC with a relatively high concentration of PA in L_d/L_o phase-separated GUVs, the PA excluded cholesterol from the L_o phase, forming an S_o phase. The S_o phase is densely packed with saturated phospholipids, exhibits high rigidity, and forms anisotropic domains.[40] Thus, we hypothesized that the anchoring of EGFP–lipids with long chains (*i.e.* EGFP–C20/C22) can induce membrane rigidification even at lower concentrations because of external insertion of saturated fatty acids into the membrane, in turn leading to suppression of the intracellular transport of the EGFP–lipid. To examine this hypothesis, first, the relationship between the alkyl chain length of fatty acids inserted into lipid membranes and domain rigidity was evaluated using phase-separated GUVs. Compared with GUVs formed from DOPC/DPPC/cholesterol = 40 : 40 : 20, in GUVs with composition DOPC/DPPC/cholesterol/PA = 40 : 20 : 20 : 20, more than half of the L_o phase changed to S_o phase (Fig. S5d and g), consistent with previous studies.[40] On substituting DPPC with behenic acid (BA, C22 : 0), >80% of the L_o phase changed to S_o phase when the GUV composition was DOPC/DPPC/cholesterol/BA = 40 : 30 : 20 : 10 (Fig. S5c and h). However, no transition from the L_o phase to
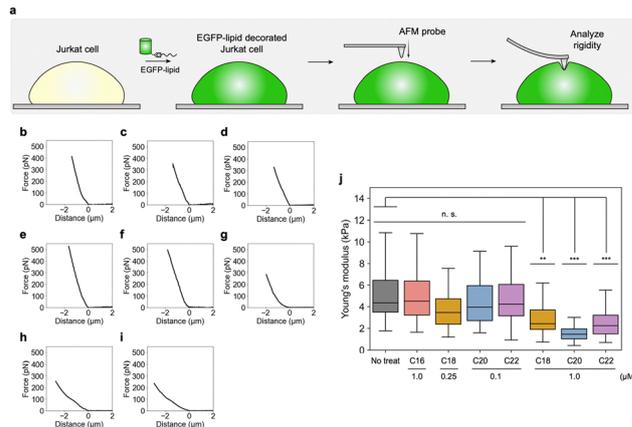
Fig. 3 Measurement of Young's modulus on Jurkat cells by atomic force microscopy (AFM). (a) Schematic illustration of the experimental setup. (b)–(i) Typical resulting force curves for cells (b) without treatment or after treatment with (c) EGFP–C16 (1.0 μM), (d) EGFP–C18 (0.25 μM), (e) EGFP–C20 (0.1 μM), (f) EGFP–C22 (0.1 μM), (g) EGFP–C18 (1.0 μM), (h) EGFP–C20 (1.0 μM), and (i) EGFP–C22 (1.0 μM), all conducted in phosphate-buffered saline at 37 °C. (j) Box plots of Young's modulus calculated by fitting the force curves using the Hertz model. The labels on the abscissa denote the type of the lipid bound to the EGFP and the EGFP–lipid concentration. $N = 50$; mean ± SE; significance is indicated as: **$p < 0.01$, ***$p < 0.001$; "n.s." indicates not significant (one-way ANOVA followed by Tukey's *post-hoc* test).

the S_o phase was observed with composition DOPC/DPPC/cholesterol/BA = 40 : 35 : 20 : 5 (Fig. S5b and h). This observation suggests that a considerable level of lipid insertion is necessary to induce domain rigidification by saturated fatty acids with long alkyl chains, even though they exhibit higher affinity for DPPC and can promote rigidification by effectively excluding cholesterol from the DPPC-rich phase of the membrane. Therefore, in our cellular experiments, where the density of EGFP–lipids localized on plasma membranes is expected to be much lower, such membrane rigidification may be limited or negligible in the experimental conditions.

On the basis of the findings in this model system, where domain rigidity was evaluated based on domain shape in GUVs, we attempted direct measurement of the rigidity of the plasma membrane of Jurkat cells associated with EGFP–lipids by using atomic force microscopy (AFM) (Fig. 3a). The AFM probe approached the center of a single cell and applied vertical pressure to the plasma membrane. Upon contact of the probe with the cell (distance = 0 nm), a repulsive force was detected, as shown in the distance–force curve (Fig. 3b–i). The increase in force relative to the pressing distance was fitted using the Hertz model to calculate the Young's modulus of the plasma membrane (Fig. 3j). The Young's modulus of the plasma membrane (no treatment group) was 5.06 ± 0.33 kPa (Fig. 3b and j), which is a reasonable value considering previous studies.[41] There was no significant difference in the Young's moduli of the plasma membranes after association with EGFP–lipids in the experimental conditions used in Fig. 2c (Fig. 3c–f and j). These results suggest that, in the present experimental conditions, the observed inhibition of the internalization of

EGFP–lipids with long lipid chains was not caused by rigidification of the plasma membrane. EGFP–lipids with longer alkyl chains potentially make cell membranes rigid, but the membrane association density in our experimental conditions is not sufficient to cause membrane rigidification. In fact, exposure to high concentrations of EGFP–C18, –C20, and –C22 resulted in a decrease in the Young's moduli of the plasma membrane (Fig. 3g–i, j and Fig. S2a), rather than an increase linked to membrane rigidification. The reduction in Young's modulus may be explained by multilayer adsorption and aggregation of lipidated proteins with long saturated fatty acids on the plasma membrane, forming a soft layer into which the AFM cantilever readily penetrated, leading to a lower apparent modulus.

Characterization of EGFP–lipid aggregation in aqueous solution

Inspired by the AFM observations following exposure of cells to high concentrations of EGFP–C18, –C20 and –C22 (Fig. 3g–j), we hypothesized that the suppressed intracellular transport of these protein–lipid fusions with long alkyl chains may be attributable to a propensity for aggregation of the EGFP–lipid on the plasma membrane. Therefore, we investigated the aggregation tendency of EGFP–lipids (EGFP–C16, –C18, –C20, –C22) in solution by examining their morphology and surface activity. Firstly, physicochemical properties of several series of lipid–peptide (lipid–G_3S–RHK–NH_2) and EGFP–lipid were determined by surface tension measurements (Fig. S6 and S7 and Tables S1 and 2). The critical aggregation concentration (CAC) of both the lipid–G_3S–RHK–NH_2 and EGFP–lipid series decreased with increasing alkyl chain length. The CAC of EGFP–lipid was decreased compared with that of lipid–G_3S–RHK–NH_2 at the same alkyl chain length, indicating enhanced aggregation propensity due to the presence of EGFP. To understand the adsorption behavior, we estimated the molecular area of EGFP at the air–liquid interface. EGFP has a barrel-shaped structure with a length of 4.2 nm and a diameter of 2.4 nm,[42] and its estimated area per molecule is 452 $Å^2$ when it is packed tightly at the air–liquid interface (Fig. S8). However, the experimental values of area per molecule were lower than the theoretical values, suggesting that the mode of adsorption of EGFP at the air–liquid interface is not monolayer adsorption, but that multiple EGFP–lipid molecules are involved. To assess the tendency of EGFP–lipids to aggregate, we calculated the value of the CAC/C20 ratio, where C20 is the surfactant concentration at which the surface tension is decreased by 20 mN m^{-1}

(Table 2). This value is used to determine structural factors in adsorption and micellization processes.[43] The values of CAC/C20 for EGFP–C20 and –C22 were lower than those for EGFP–C16 and –C18, suggesting that EGFP–lipids are prone to aggregation above a certain alkyl chain length.

Building on the tendency to aggregation of EGFP–lipids observed in the preceding experiments, we next evaluated the morphology and size of EGFP–lipid aggregates at concentrations above the CAC. The hydrodynamic radii of EGFP–lipid aggregates were measured at concentrations above the CAC, and peaks were observed at 10–20 nm and >100 nm for all the EGFP–lipids (Fig. S9a). It was observed that the peak above 100 nm shifted to smaller values as the alkyl chain length increased. This shift can be attributed to the increased propensity of EGFP–lipids to aggregate beyond a certain alkyl chain length, consistent with the tendency observed in the surface tension measurements. To gain a deeper understanding of the aggregation morphology of EGFP–lipids, transmission electron microscopy (TEM) images were obtained using dried aqueous solutions above the CAC, which revealed that all the EGFP–lipids formed aggregates larger than 100 nm (Fig. S9b). Furthermore, it appeared that the large aggregates showed connected spheres of 10–20 nm in diameter. The EGFP–lipid is composed of a fatty acid attached to EGFP *via* a flexible peptide linker (Fig. S10). These results suggest the formation of micelle-like structures of EGFP–lipids above the CAC in solution, and that individual micelles can be assembled to form large aggregates.

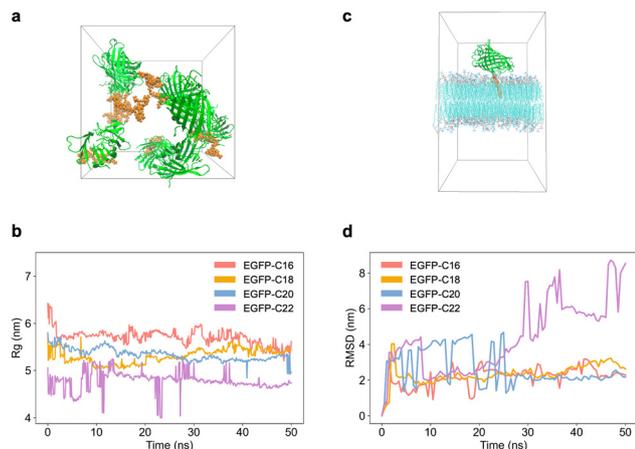## All-atom molecular dynamics (MD) simulations-based analysis of dynamic behavior of EGFP–lipid

To further investigate the aggregation behavior of EGFP–lipids observed in the experimental system, we evaluated the aggregation propensity and the membrane stability of EGFP–lipids (EGFP–C16, –C18, –C20, –C22) using all-atom molecular dynamics (MD) simulations. First, to assess the bulk aggregation behavior of EGFP–lipids, we monitored the interaction of eight EGFP–lipid molecules in water for 50 ns (Fig. 4a). Subsequently, we performed radius of gyration (R_g) analysis to calculate the distance of each atom from the center of mass of the entire protein, and evaluate the size of the aggregates (Fig. 4b). R_g values after 50 ns showed a tendency to decrease in the order of EGFP–C16 > EGFP–C18 > EGFP–C20 > EGFP–C22, with EGFP–C22 exhibiting a particularly significant reduction compared to the other alkyl chain lengths. A comparison of these simulation results with dynamic light scattering (DLS) measurements of the hydrodynamic radius (Fig. S9a)

Table 2 Physicochemical properties of EGFP–lipids based on surface tension analysis

Sample	CAC^a (μM)	σ_{min}^{b} (mN m^{-1})	Γ^{c} (mol m^{-2})	$1/\Gamma$^{d} ($Å^2$ molecule^{-1})	C20^e (μM)	pC20^f	CAC/C20
EGFP–C16	5.38	32	4.02×10^{-6}	41.3	0.73	0.31	7.73
EGFP–C18	2.83	31.2	2.96×10^{-6}	56.1	0.17	1.79	16.9
EGFP–C20	1.78	36.1	3.95×10^{-6}	42	0.35	1.04	5.01
EGFP–C22	1.6	34.8	4.88×10^{-6}	34	0.39	0.94	4.09

^{a} Critical aggregation concentration. ^{b} Minimum surface tension. ^{c} Surface excess. ^{d} Molecular occupied area. ^{e} The surfactant concentration at which the surface tension is decreased by 20 mN m^{-1}. ^{f} Negative logarithm (base 10) of the reciprocal of C20.

© 2025 The Author(s). Published by the Royal Society of Chemistry

RSC Chem. Biol., 2025, **6**, 1483–1496 | **1487**

Fig. 4 All-atom MD simulations of EGFP–lipids with different alkyl chain lengths in solution and membrane environments. (a) Snapshot of EGFP–C16 at 50 ns from an all-atom MD simulation of eight EGFP–lipid molecules in an aqueous solution. (b) Time course of the radius of gyration (R_g) of EGFP–C16, –C18, –C20, and –C22 in an aqueous solution. (c) Snapshot of EGFP–C16 at 50 ns from an all-atom MD simulation of a single EGFP–lipid molecule interacting with a lipid bilayer. (d) Time course of the root mean square deviation (RMSD) of EGFP–C16, –C18, –C20, and –C22 on a lipid bilayer.

revealed that the elongation of the alkyl chain enhances molecular interactions, thereby promoting the formation of smaller aggregates.

Next, to evaluate the behavior of EGFP–lipid molecule on lipid membranes, we tracked its fluctuations of one EGFP–lipid molecule anchored to a DPPC/cholesterol (60 : 40) lipid bilayer, as used in the SLB experiment, for 50 ns (Fig. 4c). We then performed a root mean square deviation (RMSD) analysis to calculate the fluctuations of the molecule relative to its initial state and evaluate the stability of EGFP–lipid on the lipid membrane (Fig. 4d). EGFP–C16 and EGFP–C18 were remained stably anchored to the lipid membrane throughout the 50 ns observation period. EGFP–C20 exhibited significant fluctuations during the first half of the simulation, but gradually became stable after 25 ns. In contrast, EGFP–C22 showed increasing fluctuations over time with a markedly high RMSD at 50 ns. These results indicate that EGFP–C16 and EGFP–C18 stably anchor to the lipid membrane, while the increased alkyl chain length in EGFP–C20 and EGFP–C22 significantly reduces membrane stability. This is likely due to a hydrophobic mismatch between the DPPC lipid tails and the longer alkyl chains of EGFP–C20 and EGFP–C22, resulting in thermodynamic instability.

Discussion

S-Palmitoylation is a post-translational modification that is essential for proteins to function properly on lipid membranes. *S*-Palmitoylation has been identified in a range of proteins, and

a recent database predicts that >10% of the human proteome is targeted for palmitoylation.[44] This modification is catalyzed by DHHC acyltransferases (DHHC-type PATs), of which 23 isoforms are known in humans. However, the specificity of the acyl chains that DHHC acyltransferases select as substrates is not fully understood. Although some DHHC enzymes are capable of conjugating acyl chains of different lengths to proteins, it is still unclear how the acyl chain length is regulated and affects the biological activity of the target protein.[20]

Herein, the effect of alkyl chain length on the dynamic behavior of lipidated proteins on lipid membranes was evaluated systematically from physical, chemical, and biological perspectives, using artificially lipidated proteins. A model fluorescent protein (EGFP) modified with a series of saturated fatty acids (C8–C22) was prepared to evaluate the two-dimensional behavior of the protein–lipid constructs using different artificial lipid bilayers, GUVs[45] and an SLB,[46] followed by evaluation of three-dimensional behavior through cellular experiments.

Although artificial membrane models cannot fully replicate the dynamic and heterogeneous nature of native plasma membranes, including nanoscale raft formation, protein crowding, and interactions with the cytoskeleton, they provide a controlled environment that allows molecular-level analysis of the fundamental effects of lipid modifications. In this study, we combined artificial membrane systems with cell experiments to perform a more detailed and multifaceted evaluation of how alkyl chain length influences membrane localization and intracellular transport.

The artificially lipidated proteins modified with relatively short saturated fatty acids, including those observed in naturally occurring fatty acylation (EGFP–C8, –C10, –C12, –C14), were not distributed to either artificial lipid bilayers or Jurkat cells. It is thus considered that the ability of a lipidated protein to be distributed to cells is determined by the balance of hydrophilicity and hydrophobicity of the molecule. Saturated fatty acid modifications to proteins that are shorter than palmitoylation, such as octanoylation (C8 : 0),[47] lauroylation (C12 : 0),[48] and myristoylation (C14 : 0),[2] have been reported. Among these, *N*-myristoylation (C14 : 0) is observed commonly *in vivo*. However, myristoylation alone provides only modest membrane affinity, and proteins modified with a single myristoyl fatty acid chain can reversibly associate with and dissociate from membranes.[49] Therefore, additional signals are often required to achieve stable membrane anchoring. It is assumed that proteins require the conjugation of a saturated fatty acid with at least the length of PA (C16 : 0) to localize to the membrane.

EGFP–lipids (EGFP–C18, –C20 and –C22), which were further elongated from palmitoylation, showed an increased propensity to aggregate on artificial lipid membranes and plasma membranes. In particular, EGFP–C20 and –C22 are highly prone to aggregation, as demonstrated by their surface activity in aqueous solution (Table 2). The presence of a lipid membrane may further facilitate this aggregation by serving as a scaffold, a role previously demonstrated in the membrane-assisted clustering of amphiphilic

1488 | *RSC Chem. Biol.*, 2025, **6**, 1483–1496

© 2025 The Author(s). Published by the Royal Society of Chemistry

molecules such as amyloid β.[50,51] Therefore, it is plausible that EGFP–lipids (EGFP–C18, –C20 and –C22) form aggregates on membrane surfaces even at concentrations well below their CAC in bulk solution, because interfacial aggregation below the bulk CMC has been demonstrated for surfactants.[52] This hypothesis is supported by the observed increase in the immobile fraction observed for EGFP–C20 and –C22 in FRAP experiments (Fig. 1b), as well as by a decrease in the Young's modulus of plasma membranes after exposure to EGFP–C18, –C20, and –C22, albeit at concentrations relatively high in the context of the cellular experiments (Fig. 3g–i, j and Fig. S2a). Given that the Young's modulus represents the resistance of the cell interface to deformation under vertical pressure, reduction in the Young's modulus implies the formation of a soft, protein-rich layer on the membrane, caused by multilayer adsorption and aggregation of lipidated proteins. These aggregates are not considered to alter the intrinsic mechanical properties of the plasma membrane itself, but instead act like a cushion formed on the membrane surface, reducing the repulsive force sensed by the AFM cantilever. Therefore, the observed decrease in Young's modulus is more likely to reflect the mechanical properties of the protein layer than to indicate actual softening of the membrane. Together, these results suggest that lipidated proteins can form membrane-associated aggregates even at concentrations lower than their CAC.

To further examine the molecular basis of these phenomena, we performed all-atom MD simulations using EGFP–lipids with different alkyl chain lengths (EGFP–C16, –C18, –C20, and –C22). In an aqueous solution, R_g analysis indicated that longer alkyl chains to promote more compact aggregation. On lipid bilayers, RMSD analysis revealed that EGFP–C20 and EGFP–C22 exhibited greater structural fluctuations over time, suggesting a trend toward less stable membrane anchoring. These results support the hypothesis that increased alkyl chain length promotes aggregation and suppresses lateral diffusion at membrane surfaces.
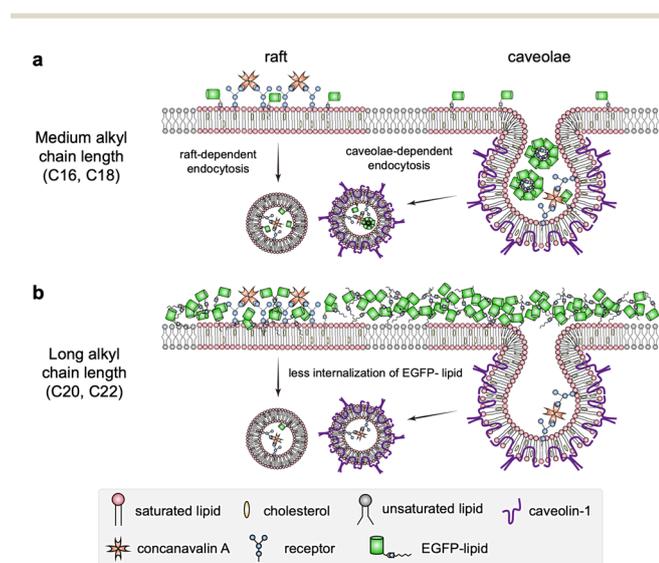
Fig. 5 shows a proposed mechanism for vesicular transport of EGFP–lipids into Jurkat cells based on the results obtained in this study. After anchoring to the plasma membrane, EGFP–C16 and –C18 were trafficked into the cell via raft accumulation and vesicular transport, associated with cytoskeletal movements induced by the multivalent binding of ConA to mannose.[37,38] Moreover, anchoring of the lipidated proteins on the plasma membrane may promote raft nucleation and growth (Fig. 5a). The scaffold protein PSD-95 in the postsynaptic membrane of neurons is thought to contribute to the maintenance of synaptic function and plasticity, and a mechanism has been proposed in postnatal developing rats in which the palmitoylation of PSD-95 is involved in domain nucleation in the postsynaptic membrane.[53] Because caveolae have a recessed structure of several tens of nanometers, it is possible that EGFP–C16 and –C18 form 10–20 nm micelles in the vicinity of the membrane and are incorporated into caveolae. In contrast, EGFP–C20 and –C22 are mostly retained in the plasma membrane, and the internalization ratio was remarkably suppressed even after immunostimulation with ConA (Fig. 2b). Although the concentration of EGFP–lipid on the cell surface was below the CAC, EGFP–C20 and –C22 appeared to form aggregates on the plasma membrane. We speculate that a large proportion of these lipidated proteins exist in an aggregated state that cannot properly anchor to raft or caveolar domains, which are typically required for endocytic uptake (Fig. 5b). Consequently, the number of proteins that can access these microdomains and subsequently undergo internalization is markedly reduced.

Our systematically designed artificial model system revealed that EGFP–C16, which mimics palmitoylation in vivo, exhibited dynamic behavior in all conditions, while EGFP–C18, which is observed as stearoylation[54,55] in vivo, exhibited dynamic behavior in certain conditions. Interestingly, EGFP–C20 and –C22 (i.e., protein modified with long-chain saturated fatty acids that are not observed in vivo), showed greatly slowed dynamic behavior on lipid membranes. It is possible that long-chain fatty acids such as arachidic acid (C20) and BA (C22) are not selected for lipid modification of natural proteins to prevent the aggregation of proteins in the vicinity of the plasma membrane. Indeed, a variety of fatty acid acyl CoAs exist in cells, including not only C16:0 and C18:0, but also those with long-chain acyl groups of C20 and above.[56] Recent studies have shown that certain DHHC acyltransferases selectively catalyze the modification of PA (C16:0) among diverse fatty acid acyl CoAs.[57] Furthermore, analysis of acyl groups conjugated to S-acylated proteins in platelets revealed that 74% were derived from PA (C16:0), 22% from stearic acid (C18:0), and 4% from oleic acid (C18:1).[58] Thus, the palmitoyl group enables proteins to express their functions properly on lipid membranes and is preferentially selected among the various fatty acids.

Although palmitoylation has been observed in a wide variety of natural proteins, the details of the mechanism of the effect of palmitoylation upon the modified protein and its application to drug discovery have not been fully investigated. While the difference in the number of carbons is slight chemically, here,

Fig. 5 Hypothesized model of cellular uptake of (a) EGFP–C16/C18 and (b) EGFP–C20/C22 following the activation of Jurkat cells by ConA.

© 2025 The Authors(s). Published by the Royal Society of Chemistry

RSC Chem. Biol., 2025, **6**, 1483–1496 | **1489**

only the artificially lipidated protein that mimicked palmitoylation exhibited dynamic behavior on lipid membranes under all experimental conditions in this study. Modification with a short fatty acid resulted in failure of association of the lipidated protein with lipid membranes, while modification with long fatty acids, which is not observed *in vivo*, limited the dynamic behavior of the product protein–lipids on lipid membranes *via* the formation of aggregates. The current system enables evaluation of how lipid structure affects protein behavior at the membrane surface under controlled extracellular conditions. However, it does not reproduce the physiological lipidation processes that occur in the cytosol. The development of intracellular MTG-based lipidation systems in the future may allow for more physiologically relevant assessments and expand the potential applications of this platform. Additional studies are necessary to determine the fate of lipidated proteins after cellular uptake, but the basic findings obtained in this study may contribute to our understanding of the significance of palmitoylation *in vivo*. The method using the LQ tag and MTG is, in principle, applicable to a wide range of soluble proteins. To further assess the generalizability of our findings, future studies could apply this system to naturally lipidated proteins such as Ras proteins and Src family proteins. They may also have important implications for the engineering of artificial lipid bilayers and plasma membranes using artificial lipidation techniques.

Conclusions

The dynamic behavior of lipidated proteins on lipid membranes plays an important role in cells. The significance of the alkyl chain length of lipidated proteins is not completely understood because of the limitations of conventional biological methods for evaluating such proteins. Here, by virtue of a simple chemical handle, we explored the behavior of artificially lipidated proteins when they are placed on phase-separated artificial biomembranes and on the plasma membrane of Jurkat cells. Our results demonstrate that altering the lipid moiety of lipidated proteins markedly affects the lipid–lipid interaction and vesicular trafficking on lipid membranes. EGFP–C16 exhibited highly dynamic lateral diffusion on artificial lipid membranes and internalized into Jurkat cells *via* raft/caveolae-dependent endocytosis in response to immunostimulation. However, artificially lipidated proteins with shorter alkyl chain lengths than PA were not able to distribute to lipid membranes, while elongation of the alkyl chain length from palmitoylation (*i.e.*, C16) suppressed two-dimensional diffusion on an SLB and three-dimensional vesicular transport into Jurkat cells. The findings obtained using our system may contribute to understanding of the significance of natural selection of lipid molecules for protein lipidation *in vivo*. In addition to providing mechanistic insights, this study offers practical guidance for designing lipid structures in applications involving artificially lipidated proteins. Our system also enables site-specific conjugation of structurally diverse lipids, including branched chains, sterol-based moieties such as cholesterol and

tocopherol, and polyunsaturated fatty acids. The ability to control membrane anchoring and dynamics by modulating lipid structure holds promise for various applications, including liposomal drug delivery, cell surface engineering, and the development of synthetic biological systems associated with membranes.

Experimental section

Materials

All reagents and solvents were used without further purification. Dichloromethane (DCM), *N*,*N*-dimethylformamide (DMF), *N*,*N*-diisopropylethylamine (DIPEA), 1-[bis(dimethylamino)methyliumyl]-1*H*-benzotriazole-3-oxide hexafluorophosphate (HBTU), 1-hydroxy-1*H*-benzotriazole hydrate (HOBt·H$_2$O), piperidine (PPD), trifluoroacetic acid (TFA), 9-fluorenylmethyloxycarbonyl (Fmoc)–Arg(Pbf)–OH, Fmoc–Gly–OH, Fmoc–His(Trt)–OH, Fmoc–Lys(Boc)–OH, Fmoc–Ser(*t*Bu)–OH, and Fmoc–Lys(Mmt)–OH were purchased from Watanabe Chemical Industry (Hiroshima, Japan). Rink amide AM resin (200–400 mesh) was purchased from Merck Millipore (Burlington, MA, USA). Arachidic acid, triisopropylsilane (TIS), acetonitrile [ACN; high-performance liquid chromatography (HPLC) grade], diethyl ether, *n*-dodecyl-β-D-maltopyranoside (DDM), octanoic acid, myristic acid, and 4% paraformaldehyde phosphate buffer solution were purchased from Wako (Osaka, Japan). Palmitic acid and stearic acid were purchased from Nacalai Tesque (Kyoto, Japan). Lauric acid, decanoic acid, BA, and ninhydrin were purchased from Tokyo Chemical Industry (Tokyo, Japan). Reagents for the Kaiser test was purchased from Kokusan Chemical (Tokyo, Japan). α-Cyano-4-hydroxycinnamic acid (CHCA) and ConA were purchased from Sigma–Aldrich (St. Louis, MO, USA). *N*-Ethylmaleimide was obtained from Kishida Chemical (Osaka, Japan). Recombinant MTG[59] and EGFP[60] fused with the LLQG sequence at the *C*-terminus (EGFP–LQ) were expressed in *Escherichia coli* using pET-22b(+) as the expression vector, according to our previous reports (Table S2). The volumetric activity (U mL^{-1}) of MTG was measured according to a previous report.[61] The concentration of EGFP–LQ was determined by the absorbance at 488 nm using an extinction coefficient of 55 000 M^{-1} cm^{-1} and a NanoDrop ND-2000 spectrophotometer (Thermo Fisher Scientific, Waltham, MA, USA). The zwitterionic saturated lipid DPPC, the zwitterionic unsaturated lipid DOPC, and cholesterol were purchased from Avanti Polar Lipids (Alabaster, AL, USA). Rhodamine–DHPE, Roswell Park Memorial Institute (RPMI)-1640 medium, Alexa Fluor 594-conjugated CT-B, human caveolin-1 siRNA (ID: s526184), Silencer™ Select Negative Control No. 1 siRNA, TRIzol, and Powerup SYBR Green Master Mix were purchased from Thermo Fisher Scientific. A PrimeScript™ RT Reagent Kit with gDNA Eraser (Perfect Real Time) was purchased from Takara Bio (Shiga, Japan). The oligonucleotide DNA for PCR primers was synthesized by FASMAC Co. Ltd (Kanagawa, Japan).

Fmoc solid phase peptide synthesis

Lipid–G$_3$S–RHK–NH$_2$ (Fig. S11) was manually synthesized by standard Fmoc solid-phase peptide synthesis. Rink amide AM

resin (0.2 mmol for lipid–G$_3$S–RHK–NH$_2$) loaded in an empty PD-10 column (GE Healthcare, Little Chalfont, UK) was pre-swollen in DCM for 30 min. The N-terminal Fmoc protecting group of the swollen resin was removed by soaking in 20% PPD in DMF for 10 min. The deprotected resin was washed with DMF (3 × 4 mL). The Fmoc deprotection was confirmed by a positive ninhydrin test. The Fmoc-protected amino acid (0.6 mmol, 3 equiv. to the loaded resin) was first activated in a coupling cocktail containing HBTU (3 equiv.), HOBt (3 equiv.), and DIPEA (6 equiv.) in DMF, then added to the resin for a 60-min coupling. The resin was washed with DMF (3 × 4 mL) and DCM (3 × 4 mL). Completion of the reaction was confirmed by a negative ninhydrin test. The process of Fmoc-group deprotection and subsequent Fmoc-protected amino acid coupling was repeated until the last amino acid residue was coupled. The resin-bound NH$_2$–peptides were coupled with lipids (10 equiv.) in a coupling cocktail for 6 h. After confirmation of lipid attachment by a negative ninhydrin test, the resin was washed with DMF (3 × 4 mL), DCM (3 × 4 mL), DMF/DCM (1 : 1; 3 × 4 mL), and methanol (3 × 4 mL), and soaked in methanol for 30 min. The shrunken resin was dried under reduced pressure for 60 min. Cleavage of peptides from the resin was conducted by soaking the resin in a solution of TFA/H$_2$O/TIS (95 : 2.5 : 2.5) for 120 min. The filtrate was concentrated by evaporation under reduced pressure and precipitated with cold diethyl ether (3 × 30 mL). The obtained crude peptides were dried at room temperature (ca. 20 ± 3 °C). The crude peptides were dissolved in ACN/water (30 : 70, 0.1% TFA).

Mass spectrometry and reverse phase-high-performance liquid chromatography (RP-HPLC) analysis of peptide amphiphiles

All the obtained peptides were colorless solids, and the yields were not determined. The synthesized peptides were identified by matrix-assisted laser desorption/ionization time-of-flight mass spectrometry (MALDI-TOF-MS). Peptide solutions were spotted on a CHCA matrix, and mass spectra were obtained using a Bruker Autoflex max MALDI-TOF mass spectrometer (Billerica, MA, USA) in positive ion detection mode. Theoretical masses were calculated using the program ChemDraw (Cambridge Soft Corporation, Waltham, MA, USA). The purity of peptides was determined by RP-HPLC analysis. HPLC was conducted using an Agilent 1260 Infinity II LC system (Agilent Technologies, Santa Clara, CA, USA). In the RP-HPLC, 1.0 mM peptide (lipid–G$_3$S–RHK–NH$_2$) in ACN/water (30 : 70, 0.1% TFA) was injected into an Inertsil ODS-3 (4.6 × 250 mm) column (GL Science, Tokyo, Japan). The analysis conditions were: flow-rate, 1.0 mL min^{-1}; detection wavelength, 280 nm; gradient, ACN/water (0.1% TFA) = 30 : 70 to 90 : 10 over 60 min. Data for lipid–G$_3$S–RHK–NH$_2$ constructs are shown in Fig. S12 (MALDI-TOF-MS, RP-HPLC).

Critical aggregation concentration (CAC) measurements of lipid–G$_3$S–RHK

The CACs of lipid–G$_3$S–RHK were measured by the pyrene 1 : 3 ratio method.[62] Lipid–G$_3$S–RHK (100 μL, 0–1.0 mM) in PBS(−) was incubated in a glass microtube containing pyrene (200 pmol)

for 60 min at 25 °C. Samples were prepared for three parallel analyses. The incubated peptides (50 μL) were put into a 96-well black half-area plate (Grainer Bio One, Kremsmünster, Austria), and fluorescence was measured using a microplate reader (SpectraMax® i3x, Molecular Devices, Tokyo, Japan) with conditions: excitation wavelength, 335 nm; emission wavelengths, 373 and 385 nm (whose intensities are abbreviated as I373 and I385 respectively); and slit, 15 nm. Plots of I373/I385 (pyrene 1 : 3 ratio) versus concentration were generated (Fig. S6) and CACs (Table S1) were determined from the intersection points of the straight lines.

MTG-mediated crosslinking reaction of EGFP–LQ with lipid–G$_3$S–RHK

The crosslinking reaction catalyzed by MTG was performed by mixing EGFP–LQ (10 μM), lipid–G$_3$S–RHK (100 μM), DDM (1% w/v), and MTG (0.1 U mL^{-1}) in 10 mM Tris–HCl buffer (pH 8.0) for 60 min at 37 °C. The reaction was terminated with N-ethylmaleimide (1 mM), and then the mixture was purified using a Ni–NTA slurry (GE Healthcare) to remove unreacted lipid–G$_3$S–RHK, MTG, and DDM. The EGFP–lipid conjugates bind to Ni–NTA because the EGFP is expressed with a His-tag, which has a strong affinity for the nickel ions immobilized on the Ni–NTA resin. Before use, the Ni–NTA slurry (50 μL) was washed with water and equilibrated with binding buffer (300 μL; 20 mM Tris–HCl, 500 mM NaCl, 20 mM imidazole; pH 7.4). Every rinsing step was carried out five times. Equilibrated slurry (500 μL) was added to the terminated reaction solution (500 μL) and incubated for 60 min at 4 °C with gentle shaking. The slurry bound to the EGFP–lipid conjugates was rinsed with binding buffer (300 μL) and was eluted with elution buffer (180 μL; 20 mM Tris–HCl, 500 mM NaCl, 1 M imidazole; pH 7.4). The eluted EGFP–lipid conjugates were desalted in a PD SpinTrap G-25 column (GE Healthcare) with PBS(−) (pH 7.4). The concentrations of the obtained conjugates were determined based on the absorbance at 488 nm using an extinction coefficient of 55 000 M^{-1} cm^{-1} and a NanoDrop ND-2000 spectrophotometer. Aliquots of the purified conjugates (10 μM, 30 μL) were injected into an Inertsil ODS-3 (4.6 × 250 mm^2) column for RP-HPLC analysis. In the RP-HPLC, water and ACN containing 0.1% TFA were used, and the analysis conditions were: flow-rate, 1.0 mL min^{-1}; detection wavelength, 280 nm; gradient, ACN/water (0.1% TFA) = 30 : 70 to 90 : 30 over 60 min. The conversion rate (purity) was determined by the ratio of the integrated peaks of unreacted EGFP and EGFP–lipid conjugates using eqn (1):

$$\text{Conversion rate (\%) = Peak area}_{\text{EGFP–lipid}}$$
$$\times 100/(\text{Peak area}_{\text{EGFP–LQ}} + \text{Peak area}_{\text{EGFP–lipid}}) \quad (1)$$

The purified conjugates (10 μM, 1 μL) were spotted on a CHCA matrix and analyzed by MALDI-TOF-MS (Fig. S13). The identity of the reaction products was confirmed by the theoretical increase in mass (Δ_{theo}) from unreacted EGFP–LQ. The mass difference (Δ) was the result of subtraction of the mass of the MTG reaction products from the mass of unreacted

© 2025 The Author(s). Published by the Royal Society of Chemistry

RSC Chem. Biol., 2025, **6**, 1483–1496 | **1491**

EGFP–LQ. In all the obtained MALDI-TOF-MS results, Δ matched Δ_{theo} within $\pm$ 100.

Critical aggregation concentration measurements of EGFP–lipid conjugates

EGFP–lipid (100 μL) solution was aspirated with a plastic syringe. The shape of the sample droplet hanging from the tip of the needle was captured by a charge-coupled device camera for 3.0×10^3 s using a DSA25 drop shape analyzer (KRÜSS, Hamburg, Germany). The surface tension was calculated using the Young–Laplace method, and the average of the last 10 points of the measured surface tension value was used as the static surface tension. For each EGFP–lipid, a static surface tension *versus* concentration graph was created, and a straight line was calculated near the CAC. The minimum surface tension of each EGFP–lipid conjugate, σ_{min} (mN m^{-1}), was calculated using the average value of the point at which the surface tension became constant. The CAC was calculated from the intersection of the straight lines. The estimated surface excess, Γ (mol m^{-2}), and the molecular occupied area, $1/\Gamma$ (Å^2 molecule^{-1}), were calculated using eqn (2), obtained from the Gibbs adsorption equation.

$$\left(\frac{\mathrm{d}\gamma}{\mathrm{d}\ln c}\right) = -RT\Gamma \qquad (2)$$

g, surface tension (mN m^{-1}); c, concentration (mol L^{-1}); T = 300 K; R = 8.31×10^3 Pa L K^{-1} mol^{-1}.

Dynamic light scattering (DLS) measurements

DLS measurements using a Zetasizer Nano ZS (Malvern, UK) were performed on EGFP–LQ (10 μM), EGFP–C16 (6 μM), EGFP–C18 (4 μM), EGFP–C20 (3 μM), and EGFP–C22 (3 μM) to analyze the hydrodynamic radii of EGFP–lipid aggregates.

Transmission electron microscopy observations

EGFP–lipid conjugates (10 μM, 2 μL) were cast on a hydrophilic carbon-coated copper grid for 2 min, followed by washing with Milli-Q water (18.2 MΩ cm; 5 μL) twice. Then, the grids were stained with 2% uranyl acetate solution for 2 min. The grids were dried in a desiccator overnight and observed using a JEM-2010 electron microscope (JEOL, Tokyo, Japan).

Preparation of giant unilamellar vesicles (GUVs)

GUVs were prepared by using a natural swelling method and exchanging the external water phase. Phospholipids, cholesterol, and fluorescent probe (rhodamine–DHPE) were dissolved in a 2 : 1 (v/v) chloroform/methanol solution to give concentrations of 2 mM for the phospholipids and cholesterol and 0.1 mM for the fluorescent probe. Lipids and cholesterol were mixed at the desired ratios to give a total volume of 20 μL. The rhodamine–DHPE was added for confocal microscopy observations. The organic solvent was evaporated under a flow of nitrogen gas, and the lipids were further dried in a vacuum desiccator for 3 h. The lipid films were hydrated with Milli-Q water (200 μL) or sorbitol aqueous solution (300 mM, 200 μL) for >6 h at 55 °C. The final lipid concentration was 0.2 mM.

The rhodamine–DHPE concentration was 1 μM. PBS(−) (1 mL) was added to the GUV suspension hydrated with sorbitol solution and stirred. The suspension was centrifuged at $800 \times g$ for 5 min at 25 °C. The supernatant was removed, PBS(−) (200 μL) was added, and the mixture was stirred to exchange the outer aqueous phase with PBS(−). DPPC and DOPC were selected as representative phosphatidylcholines, because they are major components of biological membranes and are commonly used in model systems.[30]

Microscopic observation of domain formation in fatty acid-containing lipid membranes

GUV suspension was placed on a glass coverslip, which was then covered with another smaller coverslip. The GUVs were observed using a fluorescence microscope (BZ-X800; KEYENCE, Osaka, Japan) at room temperature. To avoid photoinduced oxidation during the observation, we limited the observation time to 90 s, and ignored domains that appeared after excitation light irradiation.

Association of EGFP–lipids with GUVs

EGFP–lipids (10 μM, 1 μL) were added to GUV suspension (9 μL) to make the total volume 10 μL and the mixture was incubated for 10 min at room temperature.

Microscopic observation of GUVs associated with EGFP–lipids

Suspension of GUVs with associated EGFP–lipids was placed on a glass coverslip, which was then covered with another smaller coverslip. The GUVs were observed using CLSM (LSM700, Carl Zeiss, Oberkochen, Germany) with diode lasers (488 nm for EGFP, 555 nm for rhodamine). The observations were performed at room temperature.

Formation of supported lipid bilayers (SLBs) and association of EGFP–lipid

DPPC and cholesterol were dissolved in a 2 : 1 (v/v) chloroform/methanol solution, to give concentrations of 1 mM. The organic solvent was evaporated under a flow of nitrogen gas, and the lipids were further dried in a vacuum desiccator for 3 h. The lipid films were hydrated with Milli-Q water (1 mL). Subsequently, small unilamellar vesicles (SUVs) were prepared by extruding the suspension five times through a 100-nm polycarbonate membrane filter using the Mini-Extruder Set (Avanti Polar Lipids), with the size homogenized to 100 nm. SLBs were formed by adding SUV (200 μM, 100 μL) suspension to holes surrounded by double-sided tape on a piranha-washed cover glass and incubation at 50 °C for at least 30 min. EGFP–lipids (100 μL) were added and incubated at room temperature for 15 min. Fluorescence recovery after photobleaching was performed using CLSM following three washings in PBS(−) with the following setup: EGFP–C16: 1 μM, EGFP–C18: 0.5 μM, EGFP–C20: 1.5 μM, EGFP–C22: 1.5 μM; 488-nm laser; bleaching area: 9.9 μm^2; bleaching time: 2.2 s. The time point t = 0 was defined as the moment immediately after photobleaching. To correct for overall fluorescence fluctuations, a nonbleached reference region was monitored in parallel during the time

Paper

course measurement. The intensity in the bleached region at each time point was then normalized by the corresponding change rate observed in the nonbleached region. The resulting normalized fluorescence intensity, $FI(t)$, was fitted to eqn (3).[63] In this model, $FI(0)$ denotes the normalized fluorescence intensity immediately after bleaching, and A is a fitting coefficient. The fluorescence intensity at infinite time, corresponding to the recovery plateau, is given by $FI(\infty) = FI(0) + A$. Based on the obtained fitting parameter τ_D, the diffusion coefficient D was calculated according to eqn (4). The immobile fraction was calculated according to eqn (5), using the normalized fluorescence intensities immediately after bleaching [$FI(0)$] and after recovery [$FI(\infty)$]. This reflects the proportion of molecules that remained immobile during the observation period.

$$FI(t) = FI(0) + A \cdot e^{-\frac{2\tau_D}{t}} \left(I_0\left(\frac{2\tau_D}{t}\right) + I_1\left(\frac{2\tau_D}{t}\right) \right) \quad (3)$$

$$D = \frac{r^2}{4\tau_D} \quad (4)$$

$$\text{Immobile fraction} = \frac{1 - FI(\infty)}{1 - FI(0)} \quad (5)$$

A: fitting coefficient; τ_D: diffusion time; I_0, I_1: modified spherical Bessel functions; D: diffusion coefficient; r: radius of photobleached region.

Cell culture

Jurkat cell line RCB0806 (an immortalized line of human T lymphocytes derived from a patient with T-cell leukemia) was provided by the RIKEN BRC through the National Bio-Resource Project of MEXT, Japan, and cultured in RPMI-1640 medium. The medium was supplemented with 10% fetal bovine serum, and cells were cultured in a humidified incubator at 37 °C in the presence of 5% CO_2.

Transfection of siRNA into Jurkat cells

Transfection of siRNA into Jurkat cells was performed using the Neon transfection system (Thermo Fisher Scientific); 2.0×10^6 cells suspended in resuspension buffer containing 100 pmol siRNA were transfected at 1400 V, with 10-ms pulse width, and three pulses. The cells were then incubated at 37 °C in the presence of 5% CO_2 for 48–72 h.

Real-time reverse transcription-PCR

Total RNA was isolated from cell suspension using TRIzol™ according to the manufacturer's manual. Genomic DNA removal and reverse transcription reactions were performed using a PrimeScript™ RT Reagent Kit with gDNA Eraser according to the manufacturer's manual. The synthesized cDNA was mixed with respective primer pairs[64] (Table S3) and Powerup SYBR Green Master Mix, then quantitative PCR analysis was conducted using a real-time PCR system (Applied Biosystems, Thermo Fisher Scientific). Expression of the human β-actin gene was detected as an internal control. The number of cycles required to amplify the target gene was determined, and the

relative expression of the target gene was calculated as follows: individual threshold cycles (CT) from the experimental or control group were normalized by the CT for β-actin, and two raised to the power of negative ΔΔCT (experimental cells) was divided by two raised to the power of negative ΔΔCT (control cells).

Staining of lipid rafts

CT-B is a fluorescent probe that interacts with monosialotetrahexosyl ganglioside (GM1) and is used to label lipid rafts. Cells were blocked with bovine serum albumin [0.02% (v/v)] in PBS(−) on ice for 30 min followed by incubation at 37 °C in the presence of 5% CO_2 for 10 min with CT-B (1 μg mL^{-1} dissolved in PBS(−)), and then washed twice with PBS(−).

Association of EGFP–lipids to Jurkat cells

EGFP–lipid (10 μM) was added to cell suspensions at a final concentration of 0.1, 0.25, 0.5, or 1.0 μM. The cells were incubated at 37 °C in the presence of 5% CO_2 for 15 min and then washed twice with PBS(−).

Activation of Jurkat cells by addition of ConA

ConA discriminates between glycoproteins in the membrane and α-linked mannose in the serum. It induces immune activation in Jurkat cells and triggers raft internalization and clustering.[37,38] Activation of Jurkat cells was performed by the action of ConA (10 μg mL^{-1}). ConA was added to cell suspensions at the time of observation.

Microscopic observation of Jurkat cells associated with EGFP–lipids

Jurkat cells were incubated in 4% paraformaldehyde phosphate buffer solution at room temperature for 15 min and washed twice with PBS(−) before CLSM observation. The internalization ratio of fluorescent molecules was calculated by using ZEN Microscopy Software (Carl Zeiss, Oberkochen, Germany).

Cytotoxicity assay of EGFP–lipid

Jurkat cells (2.0×10^4 cells per well, 50 μL in PBS(−)) were seeded into a clear 96-well tissue culture plate. EGFP–lipid (final concentration: 1 μM) was added to each well and incubated for 15 min. After incubation, 50 μL of culture medium was added to each well, followed by 10 μL of Cell Counting Kit-8 reagent (WST-8; Dojindo Laboratories). The plate was then incubated at 37 °C with 5% CO_2 for 3 h. Cell viability was subsequently assessed by measuring the absorbance at 450 nm using a microplate reader. Viability was calculated using eqn (6), with the blank defined as PBS(−) and WST-8 without cells. Absorbance measurements were performed in triplicate using independently prepared samples.

$$\text{Cell viability (\%)} = \frac{OD_{450}(\text{sample}) - OD_{450}(\text{blank})}{OD_{450}(\text{control}) - OD_{450}(\text{blank})} \times 100 \quad (6)$$

Measurement of Young's modulus of Jurkat cells with associated EGFP–lipids by atomic force microscopy (AFM)

Jurkat cells were incubated with 1 μM EGFP–lipid in PBS(−) for 15 min, followed by washing with PBS(−) at least twice. Measurements of the Young's modulus of cells were conducted

© 2025 The Author(s). Published by the Royal Society of Chemistry

RSC Chem. Biol., 2025, **6**, 1483–1496 | 1493

by using an AFM system (force spectroscopy system; CellHesion 200, JPK Instruments – Bruker Nano GmbH, Billerica, MA, USA). An AFM probe (curvature radius of tip: 20 nm; spring constant of a cantilever: 0.01 N m^{-1}; MLNV-C, Bruker) approached at a rate of 3.0 μm s^{-1} toward the center of a Jurkat cell that was placed on the bottom of a Petri dish filled with PBS($-$). Until the repulsive-force value reached a set point of 0.25 nN, a force curve was recorded. Force curves were obtained for 50 different cells and then processed using JPK Data Processing software (version 6.4; JPK Instruments – Bruker Nano GmbH) to estimate the Young's modulus of the cell membrane by fitting with the Hertz model.

MD simulation studies

MD simulations were performed using GROMACS package[65] and CHARMM-GUI[66] with the CHARMM36m force field.[67,68] The chemical structures of EGFP–lipids were obtained and optimized using MOE. CHARMM-GUI Multicomponent Assembler[69] was used to generate starting coordinates for the simulations. In the lipid membrane simulation, a bilayer containing 132 DPPC molecules and 88 cholesterol molecules in the upper leaflet and 135 DPPC molecules and 90 cholesterol molecules in the lower leaflet was constructed. The remaining contents of the cube consisted of water (TIP3P) and charge balanced with Na$^+$ and Cl$^-$. A 50-ns simulation was performed for each of the systems under periodic boundary conditions. Analysis of MD trajectories was performed using the GROMACS.

The definition of RMSD is as follows:

$$\text{RMSD} = \sqrt{\frac{1}{N}\sum_{i=1}^{N}\left(r_i^{(t)} - r_i^{(0)}\right)^2}$$

N: the number of atoms in the system being compared. $r_i^{(t)}$: The position of the i-th atom at time t (current structure in the simulation). $r_i^{(0)}$: The position of the i-th atom in the reference structure (minimized structure). $(r_i^{(t)} - r_i^{(0)})^2$: the squared difference between the positions of the i-th atom at time t and in the reference structure.

Statistical analysis

Statistical analysis was carried out using homemade Python code. Statistical significance was calculated by the unpaired t-test or Mann–Whitney U-test followed by Bonferroni correction, the Kruskal–Wallis test followed by the Dunn–Bonferroni *post-hoc* test, or Welch's t-test followed by FDR correction (Benjamini–Hochberg), or one-way ANOVA followed by Tukey's *post-hoc* test for multiple comparisons. Significance is indicated as: *$p < 0.05$, **$p < 0.01$, ***$p < 0.001$; "*n*.s." indicates not significant.

Author contributions

K. U.: data curation, formal analysis, methodology, investigation, validation, writing the original draft; N. S. and R. W.: formal analysis, methodology, writing/reviewing and editing; S. S., K. T, and N. O.: formal analysis, investigation; M. G. and M. T. (Masaru Tanaka): resources, writing/reviewing and editing; M. T. (Masahiro Takagi): conceptualization, supervision, writing/reviewing and editing. N. K.: conceptualization, methodology, validation, supervision, writing/reviewing and editing. All authors contributed to the discussion of the paper and approved the manuscript.

Conflicts of interest

There are no conflicts to declare.

Data availability

All relevant data are within the manuscript and its SI file.

Supplementary information is available. See DOI: **https://doi.org/10.1039/d5cb00143a**

Acknowledgements

Notes and references

1 C. T. Walsh, S. Garneau-Tsodikova and G. J. Gatto, *Angew. Chem., Int. Ed.*, 2005, **44**, 7342–7372.

2 H. Jiang, X. Zhang, X. Chen, P. Aramsangtienchai, Z. Tong and H. Lin, *Chem. Rev.*, 2018, **118**, 919–988.

3 D. A. Mitchell, A. Vasudevan, M. E. Linder and R. J. Deschenes, *J. Lipid Res.*, 2006, **47**, 1118–1127.

4 S. Pei and H. L. Piao, *ACS Chem. Biol.*, 2024, **19**, 1868–1882.

5 M. E. Linder and R. J. Deschenes, *Nat. Rev. Mol. Cell Biol.*, 2007, **8**, 74–84.

6 I. Leventhal, D. Lingwood, M. Grzybek, Ü. Coskun and K. Simons, *Proc. Natl. Acad. Sci. U. S. A.*, 2010, **107**, 22050–22054.

7 A. D. Goddard and A. Watts, *BMC Biol.*, 2012, **10**, 27.

8 K. Simons and E. Ikonen, *Nature*, 1997, **387**, 569–572.

9 K. Simons and D. Toomre, *Nat. Rev. Mol. Cell Biol.*, 2000, **1**, 31–41.

10 S. N. Treistman and G. E. Martin, *Trends Neurosci.*, 2009, **32**, 629–637.

11 S. Kim, B. C. Lee, A. R. Lee, S. Won and C. S. Park, *FEBS Lett.*, 2014, **588**, 713–719.

12 I. M. Ahearn, K. Haigis, D. Bar-Sagi and M. R. Philips, *Nat. Rev. Mol. Cell Biol.*, 2012, **13**, 39–51.

1494 | *RSC Chem. Biol.*, 2025, **6**, 1483–1496

© 2025 The Author(s). Published by the Royal Society of Chemistry

13 J. Jin, X. Zhi, X. Wang and D. Meng, *J. Cell. Physiol.*, 2021, **236**, 3220–3233.

14 A. Arcaro, M. Aubert, M. E. Espinosa del Hierro, U. K. Khanzada, S. Angelidou, T. D. Tetley, A. G. Bittermann, M. C. Frame and M. J. Seckl, *Cell. Signalling*, 2007, **19**, 1081–1092.

15 C. Aicart-Ramos, R. A. Valero and I. Rodriguez-Crespo, *Biochim. Biophys. Acta, Biomembr.*, 2011, **1808**, 2981–2994.

16 A. M. Zimnicka, Y. S. Husain, A. N. Shajahan, M. Sverdlov, O. Chaga, Z. Chen, P. T. Toth, J. Klomp, A. V. Karginov, C. Tiruppathi, A. B. Malik and R. D. Minshall, *Mol. Biol. Cell*, 2016, **27**, 2090–2106.

17 L. Jia, M. Chisari, M. H. Maktabi, C. Sobieski, H. Zhou, A. M. Konopko, B. R. Martin, S. J. Mennerick and K. J. Blumer, *J. Biol. Chem.*, 2014, **289**, 6249–6257.

18 J. Greaves, G. R. Prescott, Y. Fukata, M. Fukata, C. Salaun and L. H. Chamberlain, *Mol. Biol. Cell*, 2009, **20**, 1845–1854.

19 K. R. Tonn Eisinger, K. M. Woolfrey, S. P. Swanson, S. A. Schnell, J. Meitzen, M. Dell'Acqua and P. G. Mermelstein, *J. Biol. Chem.*, 2018, **293**, 15901–15911.

20 F. S. Mesquita, L. Abrami, M. E. Linder, S. X. Bamji, B. C. Dickinson and F. G. van der Goot, *Nat. Rev. Mol. Cell Biol.*, 2024, **25**, 488–509.

21 K. Uchida, H. Obayashi, K. Minamihata, R. Wakabayashi, M. Goto, N. Shimokawa, M. Takagi and N. Kamiya, *Langmuir*, 2022, **38**, 9640–9648.

22 H. Abe, M. Goto and N. Kamiya, *Chem. – Eur. J.*, 2011, **17**, 14004–14008.

23 M. Takahara, R. Wakabayashi, N. Fujimoto, K. Minamihata, M. Goto and N. Kamiya, *Chem. – Eur. J.*, 2019, **25**, 7315–7321.

24 M. Takahara, S. Mochizuki, R. Wakabayashi, K. Minamihata, M. Goto, K. Sakurai and N. Kamiya, *Bioconjugate Chem.*, 2021, **32**, 655–660.

25 P. Santoso, K. Minamihata, Y. Ishimine, H. Taniguchi, T. Komada, R. Sato, M. Goto, T. Takashima, T. Taira and N. Kamiya, *ACS Infect. Dis.*, 2022, **8**, 1051–1061.

26 H. Taniguchi, Y. Ishimime, K. Minamihata, P. Santoso, T. Komada, H. Saputra, K. Uchida, M. Goto, T. Taira and N. Kamiya, *Mol. Pharm.*, 2022, **19**, 3906–3914.

27 I. Levental, K. R. Levental and F. A. Heberle, *Trends Cell Biol.*, 2020, **30**, 341–353.

28 C. Dietrich, L. A. Bagatolli, Z. N. Volovyk, N. L. Thompson, M. Levi, K. Jacobson and E. Gratton, *Biophys. J.*, 2001, **80**, 1417–1428.

29 B. Zens, J. Sawa-Makarska and S. Martens, *Methods*, 2015, **75**, 37–43.

30 N. Shimokawa and M. Takagi, *Adv. Exp. Med. Biol.*, 2024, **1461**, 15–32.

31 A. S. Klymchenko and R. Kreder, *Chem. Biol.*, 2014, **21**, 97–113.

32 D. Axelrod, *J. Membr. Biol.*, 1983, **75**, 1–10.

33 Y. I. Henis, B. Rotblat and Y. Kloog, *Methods*, 2006, **40**, 183–190.

34 A. K. Kenworthy, B. J. Nichols, C. L. Remmert, G. M. Hendrix, M. Kumar, J. Zimmerberg and J. Lippincott-Schwartz, *J. Cell Biol.*, 2004, **165**, 735–746.

35 J. Hjort Ipsen, G. Karlstr∼m, O. G. Mouritsen, H. Wennerstr∼m and M. J. Zuckermann, *Biochim. Biophys. Acta*, 1987, **905**, 162–172.

36 Y. W. Chiangs, A. J. Costa-Filho and J. H. Freed, *J. Phys. Chem. B*, 2007, **111**, 11260–11270.

37 S. Yabuuchi, S. Endo, K. O. Baek, K. Hoshino, Y. Tsujino, M. C. Vestergaard and M. Takagi, *J. Biosci. Bioeng.*, 2017, **124**, 685–693.

38 N. Sharma, K. O. Baek, N. Shimokawa and M. Takagi, *J. Biosci. Bioeng.*, 2019, **127**, 479–485.

39 K. G. Rothberg, J. E. Heuser, W. C. Donzell, Y.-S. Ying, J. R. Glenney and R. G. W. Anderson, *Cell*, 1992, **68**, 673–682.

40 N. Shimokawa, R. Mukai, M. Nagata and M. Takagi, *Phys. Chem. Chem. Phys.*, 2017, **19**, 13252–13263.

41 L. Zhao, X. Fu, L. Zhang and Z. Ye, *Colloids Surf., B*, 2022, **218**, 112784.

42 M. A. Hink, R. A. Griep, J. W. Borst, A. Van Hoek, M. H. M. Eppink, A. Schots and A. J. W. G. Visser, *J. Biol. Chem.*, 2000, **275**, 17556–17560.

43 M. J. Rosen, *Surfactants and Interfacial Phenomena*, John Wiley and Sons, Inc., New York, 3rd edn, 2004.

44 M. Blanc, F. David, L. Abrami, D. Migliozzi, F. Armand, J. Bürgi and F. G. van der Goot, *F1000Res*, 2015, **4**, 261.

45 C. Nicolini, J. Baranski, S. Schlummer, J. Palomo, M. Lumbierres-Burgues, M. Kahms, J. Kuhlmann, S. Sanchez, E. Gratton, H. Waldmann and R. Winter, *J. Am. Chem. Soc.*, 2006, **128**, 192–201.

46 J. D. Carder, B. Barile, K. A. Shisler, F. Pisani, A. Frigeri, K. W. Hipps, G. P. Nicchia and J. A. Brozik, *J. Phys. Chem. B*, 2024, **128**, 603–621.

47 J. A. Gutierrez, P. J. Solenberg, D. R. Perkins, J. A. Willency, M. D. Knierman, Z. Jin, D. R. Witcher, S. Luo, J. E. Onyia and J. E. Hale, *Proc. Natl. Acad. Sci. U. S. A.*, 2008, **105**, 6320–6325.

48 Y. Hashimoto, T. Matsuda, Y. Matsuura, T. Haga and Y. Fukada, *J. Biochem.*, 2004, **135**, 319–329.

49 O. Gutman, G. M. Pai, I. Rubio and Y. I. Henis, *Mol. Biol. Cell*, 2016, **27**, 3926–3936.

50 M. S. Terakawa, H. Yagi, M. Adachi, Y. H. Lee and Y. Goto, *J. Biol. Chem.*, 2015, **290**, 815–826.

51 A. Khondker, R. J. Alsop, S. Himbert, J. Tang, A. C. Shi, A. P. Hitchcock and M. C. Rheinstädter, *Sci. Rep.*, 2018, **8**, 12367.

52 M. Duan, H. Wang, S. Fang and Y. Liang, *J. Colloid Interface Sci.*, 2014, **417**, 285–292.

53 K. Tulodziecka, B. B. Diaz-Rohrer, M. M. Farley, R. B. Chan, G. Di Paolo, K. R. Levental, M. Neal Waxham and I. Levental, *Mol. Biol. Cell*, 2016, **27**, 3480–3489.

54 L. V. Kordyukova, M. V. Serebryakova, L. A. Baratova and M. Veit, *J. Virol.*, 2008, **82**, 9288–9292.

55 J. Ying, Y. Yang, X. Zhang, Z. Dong and B. Chen, *Proc. Natl. Acad. Sci. U. S. A.*, 2024, **121**, e2400569121.

56 C. A. Haynes, J. C. Allegood, K. Sims, E. W. Wang, M. C. Sullards and A. H. Merrill, *J. Lipid Res.*, 2008, **49**, 1113–1125.

© 2025 The Author(s). Published by the Royal Society of Chemistry

RSC Chem. Biol., 2025, **6**, 1483–1496 | 1495

57 J. Greaves, K. R. Munro, S. C. Davidson, M. Riviere, J. Wojno, T. K. Smith, N. C. O. Tomkinson and L. H. Chamberlain, *Proc. Natl. Acad. Sci. U. S. A.*, 2017, **114**, E1365–E1374.

58 L. Muszbek, G. Haramura, J. E. Cluette-Brown, E. M. Van Cott and M. Laposata, *Lipids*, 1999, **34**, S331–S337.

59 R. Sato, K. Minamihata, R. Ariyoshi, H. Taniguchi and N. Kamiya, *Protein Expression Purif.*, 2020, **176**, 105730.

60 Y. Tanaka, Y. Tsuruda, M. Nishi, N. Kamiya and M. Goto, *Org. Biomol. Chem.*, 2007, **5**, 1764–1770.

61 H. L. Yang, L. Pan and Y. Lin, *Biosci., Biotechnol., Biochem.*, 2009, **73**, 2531–2534.

62 J. Aguiar, P. Carpena, J. A. Molina-Bolívar and C. Carnero Ruiz, *J. Colloid Interface Sci.*, 2003, **258**, 116–122.

63 D. M. Soumpasis, *Biophys. J.*, 1983, **41**, 95–97.

64 H.-Y. Lin, Y.-T. Yang, S.-L. Yu, K.-N. Hsiao, C.-C. Liu, C. Sia and Y.-H. Chow, *J. Virol.*, 2013, **87**, 9064–9076.

65 M. J. Abraham, T. Murtola, R. Schulz, S. Páll, J. C. Smith, B. Hess and E. Lindah, *SoftwareX*, 2015, **1–2**, 19–25.

66 S. Jo, T. Kim, V. G. Iyer and W. Im, *J. Comput. Chem.*, 2008, **29**, 1859–1865.

67 J. Lee, X. Cheng, J. M. Swails, M. S. Yeom, P. K. Eastman, J. A. Lemkul, S. Wei, J. Buckner, J. C. Jeong, Y. Qi, S. Jo, V. S. Pande, D. A. Case, C. L. Brooks, A. D. MacKerell, J. B. Klauda and W. Im, *J. Chem. Theory Comput.*, 2016, **12**, 405–413.

68 B. R. Brooks, C. L. Brooks, A. D. Mackerell, L. Nilsson, R. J. Petrella, B. Roux, Y. Won, G. Archontis, C. Bartels, S. Boresch, A. Caflisch, L. Caves, Q. Cui, A. R. Dinner, M. Feig, S. Fischer, J. Gao, M. Hodoscek, W. Im, K. Kuczera, T. Lazaridis, J. Ma, V. Ovchinnikov, E. Paci, R. W. Pastor, C. B. Post, J. Z. Pu, M. Schaefer, B. Tidor, R. M. Venable, H. L. Woodcock, X. Wu, W. Yang, D. M. York and M. Karplus, *J. Comput. Chem.*, 2009, **30**, 1545–1614.

69 N. R. Kern, J. Lee, Y. K. Choi and W. Im, *Nat. Commun.*, 2024, **15**, 5459.